

Micro and Macro Motility-Induced Phase Separation in a two-dimensional Active Brownian Particle system

Claudio B. Caporusso,¹ Pasquale Digregorio,^{1,2} Demian Levis,^{3,4} Leticia F. Cugliandolo,^{5,6} and Giuseppe Gonnella¹

¹*Dipartimento di Fisica, Università degli Studi di Bari and INFN, Sezione di Bari, via Amendola 173, Bari, I-70126, Italy*

²*CECAM Centre Européen de Calcul Atomique et Moléculaire, Ecole Polytechnique Fédérale de Lausanne, Batochimie, Avenue Forel 2, 1015 Lausanne, Switzerland*

³*Departament de Física de la Materia Condensada, Facultat de Física, Universitat de Barcelona, Martí i Franquès 1, E08028 Barcelona, Spain*

⁴*UBICS University of Barcelona Institute of Complex Systems, Martí i Franquès 1, E08028 Barcelona, Spain*

⁵*Sorbonne Université, Laboratoire de Physique Théorique et Hautes Energies, CNRS UMR 7589, 4 Place Jussieu, 75252 Paris Cedex 05, France*

⁶*Institut Universitaire de France, 1 rue Descartes, 75005 Paris France*

(Dated: March 8, 2022)

As a result of non-equilibrium forces, purely repulsive self-propelled particles undergo macro-phase separation between a dense and a dilute phase. We present a thorough study of the ordering kinetics of such Motility-Induced Phase Separation (MIPS) in Active Brownian Particles in two-dimensions, and we show that it is generically accompanied by micro-phase separation. The growth of the dense phase follows a law akin to the one of liquid-gas phase separation. However, it is made of a mosaic of hexatic micro-domains whose size does not coarsen indefinitely, leaving behind a network of extended topological defects from which microscopic dilute bubbles arise. The characteristic length of these finite-size structures increases with activity, independently of the choice of initial conditions.

Active systems are ubiquitous in Nature. Driven out of equilibrium by the consumption of energy from the environment, they cannot be described using the tools of equilibrium statistical physics, and present intriguing collective behavior [1, 2]. One such peculiarity is that, at sufficiently high activity, their constituents cluster in the absence of attractive interactions. A steady state with a dense droplet immersed in a dilute background can thus be reached in systems of purely-repulsive spherical particles by Motility-Induced Phase Separation (MIPS) [3].

Arguably, the simplest microscopic active matter model is one of self-propelled spheres undergoing rotational diffusion, and excluded volume interactions only. This is the Active Brownian Particles (ABP) model that exhibits a very rich phase diagram, including MIPS, especially in two dimensions ($2d$) [4–16]. In particular, the special role played by hexatic order in these systems was discussed in [10–14], and the existence of a phase with such order was exhibited [11]. In parallel to particle based models, the large scale and long time behavior of systems exhibiting MIPS were addressed with adaptations of the Cahn-Hilliard approach [9, 17–20].

While the non-equilibrium phase diagram of (hard) ABP is well established [11], the dynamics across the various phase transitions, how is the dense droplet formed via MIPS, and which is its actual nature, still need clarification. A relevant question to ask is whether the hexatic ordering helps or interferes with the simple particle aggregation. Moreover, whether the droplet behaves as a $2d$ hexatic or liquid, featuring or not gas bubbles inside [20], are important issues that have to be elucidated.

In this Letter we address these points and in so do-

ing we also clarify the origin of the cavitation gas bubbles recently predicted with a continuum description [20]. Using extensive numerical simulations (more than 10^6 ABP evolved beyond 10^8 MD-steps) we identify and

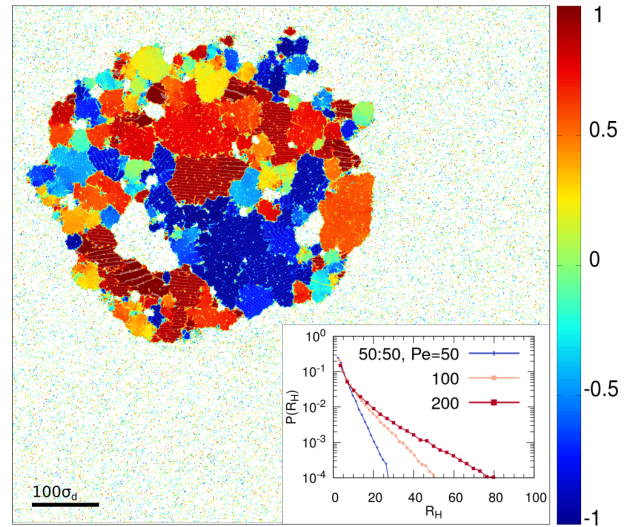


FIG. 1. Hexatic domains and bubbles in a MIPS droplet. A steady-state snapshot of 512^2 ABP at moderate density ($\phi = 0.25$) and high activity ($Pe = 200$) showing a *macro*-droplet made of a mosaic of hexatic *micro*-domains, delimited by clusters of topological defects from which *micro*-bubbles arise. The different orientational orders are indicated by the color scale associated to the projection of the local hexatic order parameter on the mean orientation. Inset: stationary distribution of hexatic domain radii for three Pe and equal fraction of dense and dilute coexisting phases.

characterize several dynamic regimes: multi-nucleation, condensation and aggregation, and coarsening fulfilling dynamic scaling, see movie 1 in the SM. Furthermore, we show that, asymptotically, the *macro*-droplet self-organizes into a mosaic of hexatic *micro*-domains, see Fig. 1. Indeed, the hexatic domains do not coarsen to reach the droplet size but rather saturate to a microscopic size that can be directly controlled by self-propulsion. Different hexatic domains are delimited by clusters of topological defects, leaving behind regions of lower density from which *micro*-bubbles are created. Devising generic mechanisms to control the spatiotemporal organization of active matter into structures that do not coarsen constitutes a central challenge of current research: such problem has been tackled with simple models of self-propelled particles with chemotactic [21, 22], competing [23, 24], or anisotropic (polar or nematic) [25–27] interactions, among others. Here we establish the existence of a structure, associated to the hexatic order, that does not coarsen, in a simpler scenario that shows *a posteriori* the need to make a connection between MIPS and $2d$ melting [11, 12, 28, 29].

We consider N particles at positions \mathbf{r}_i in an $L \times L$ box with periodic boundary conditions evolving *via*

$$\begin{aligned} \gamma \dot{\mathbf{r}}_i &= F_{\text{act}} \mathbf{n}_i - \sum_{j(\neq i)} \nabla_i U(r_{ij}) + \sqrt{2\gamma k_B T} \boldsymbol{\xi}_i, \\ \dot{\theta}_i &= \sqrt{2D_\theta} \eta_i, \end{aligned} \quad (1)$$

(see [11] for details) where F_{act} is the self-propulsion force acting along $\mathbf{n}_i = (\cos \theta_i(t), \sin \theta_i(t))$, and $U(r) = 4\varepsilon[(\sigma/r)^{64} - (\sigma/r)^{32}] + \varepsilon$ if $r < \sigma_d = 2^{1/32}\sigma$ and 0 otherwise, with $r_{ij} = |\mathbf{r}_i - \mathbf{r}_j|$. The components of $\boldsymbol{\xi}$ and η are zero-mean and unit variance independent white Gaussian noises. The units of time, length and energy are $\tau = D_\theta^{-1}$, σ_d and ε , respectively. We fix $\gamma = 10$, $k_B T = 0.05$ and $D_\theta = 3k_B T / (\sigma_d^2 \gamma) = 0.015$. We perform quenches by suddenly turning on activity, quantified by the Péclet number $\text{Pe} = F_{\text{act}} \sigma_d / (k_B T)$, deep in the MIPS coexistence region [30], on a homogeneous configuration at a given packing fraction $\phi = \pi \sigma_d^2 N / (4L^2)$. We then follow the ordering process and, in particular, we monitor the characteristic length scales of phase separation, hexatic ordering and cavitation bubbles.

The dense phase is formed through a rather complex process. First, there is multi-nucleation of many small droplets. In a second regime, small droplets evaporate while larger ones grow by condensation and aggregation. Next, a coarsening scaling limit establishes. Finally, the size of the dense cluster saturates to a value that grows with the system size L . A first measure of the typical dense phase length scale, exhibiting the three regimes, is given by the first moment of the structure factor, $S(\mathbf{k}, t) = N^{-1} \sum_{ij} e^{i\mathbf{k}(\mathbf{r}_i - \mathbf{r}_j)}$, *via* $R(t) = \pi / [\int dk k S(k, t) / \int dk S(k, t)]$. It is plotted in Fig. 2(a) for three Pe values (all lying on the 50:50-curve defined as the set of points for which the system de-mixes

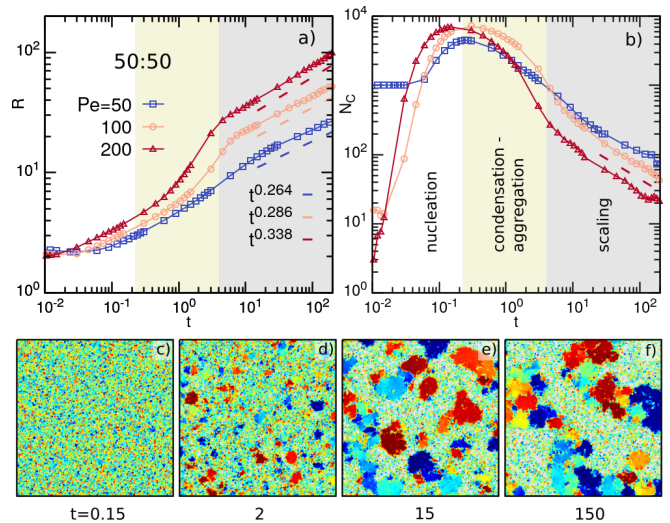


FIG. 2. **Dense phase formation.** (a) Typical size from $S(k, t)$ and (b) number of clusters, both as a function of time, after a quench into the MIPS coexistence region, in a system with $N = 1024^2$ particles at different Pe on the curve with equal surface fraction of dense and dilute phases. Three time regimes are discerned: nucleation, condensation and aggregation, and scaling. Representative snapshots with local hexatic order are shown at (c) $t = 0.15$ (nucleation), (d) 2 (aggregation), (e) 15 and (f) 150 (scaling) for $\text{Pe} = 100$.

into equal fractions of dense and dilute phases). In the first nucleation regime, R is roughly independent of Pe. The crossover to condensation and aggregation is favored by increasing Pe. Finally, R is algebraic in the scaling regime with a universal exponent $1/z$ that is closer to the expected $z = 3$ of phase separation [31] (or diffusion limited regular cluster aggregation [33]) than the values estimated in previous works [7, 10, 15] though not quite identical to it. (The dynamic scaling hypothesis [31] is fulfilled in this regime, see the SM.) Note that even in kinetic Ising models for which $z = 3$ is proven, it is notably difficult to measure it numerically [32]. The simultaneous counting of the total number of particle clusters, N_C in Fig. 2(b) (see the SM for its definition), illustrates the nature of the first two regimes. During nucleation N_C grows fast until a maximum, which signals the crossover towards aggregation and its progressive fast decay. In the scaling regime a fit to the $\text{Pe} = 200$ data yields $N_C \sim t^{-0.59}$, consistent with the growth of R .

Another measure of the dense phase size is provided by the average radius of gyration of the clusters, $R_G^2 = \langle N_d^{-1} \sum_{i \in d} (\mathbf{r}_i - \mathbf{r}_d^{\text{cm}})^2 \rangle$, with \mathbf{r}_i the position of the i th particle among the N_d ones in the cluster, and \mathbf{r}_d^{cm} the position of the cluster center of mass. $\langle \dots \rangle$ is an average over all clusters. Its behavior, in Fig. 3(a), is analogous to the one of $R(t)$. The dotted vertical lines locate the crossovers between the time-regimes in Fig. 2, with a slightly more extended intermediate one in which R_G

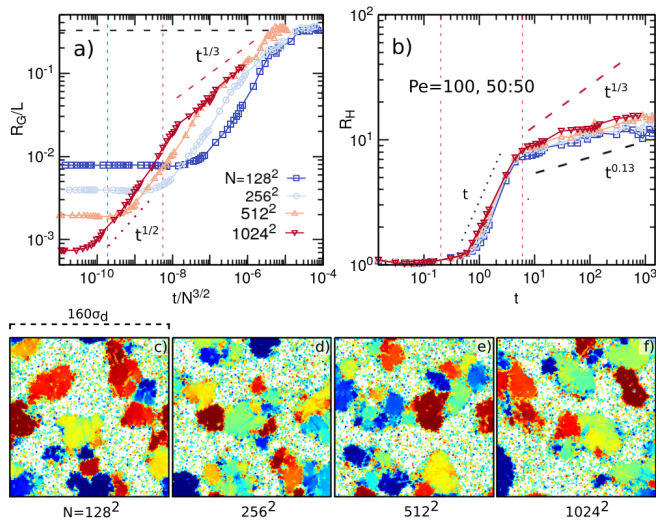


FIG. 3. Macro-droplet against hexatic micro-domains. Growth of the dense phase radius of gyration, R_G , normalized by the system size L (a) and the hexatic length R_H (b) for $Pe = 100$ and different N on the 50:50-curve. In (a), R_G/L saturates at $\sqrt{5/48}$ (a droplet that occupies half the available surface). In (b) we represent the slow growth $t^{0.13}$, and $t^{1/3}$ for comparison. The vertical dotted lines mark the crossover between the three regimes in the largest system. Below, a zoom over a sector of these systems with linear size $160\sigma_d$ taken at $t = 15$ (scaling regime) is shown.

raises with the $t^{1/2}$ of Brownian aggregation [33] to later accelerate pushed by activity, and then crossover to $t^{1/3}$ when the mass of the gas reaches its constant target value (see the SM). Due to the finite system size, R_G cannot grow indefinitely and it saturates to $R_G^s \propto L$, after the relaxation time $N^{z/2}$. The smaller the system size, the farther from $z = 3$ is the growth in the scaling regime. For the largest case, $N = 1024^2$, the data are very close to this expected value. At fixed N and t , $R_G(t)$ increases monotonically with ϕ and Pe , since the fraction of the system in the dense phase also does, see Fig. 4(a), (c).

From the previous study, one may expect any kind of length scale associated to a relevant order parameter to, depending on the quench, either grow to reach a macroscopic value $\propto L$ or, on the contrary, relax to a vanishing one. We now show that this does not apply to the hexatic order of ABP in the MIPS regime.

We attach a hexatic order parameter to each particle, $\psi_{6j} = N_j^{-1} \sum_{k \in \mathcal{D}_j} e^{i6\theta_{jk}}$, with θ_{jk} the angle formed by the segment that connects the center of the j th disk and the one of its k th, out of N_j , nearest neighbors found with a Voronoi construction. The colors in the snapshots in Figs. 1-3 represent different hexatic order. The clusters that aggregate do not necessarily share the same ψ_{6j} , and grain boundaries progressively appear in the growing dense phase. Whether they heal or not is the issue that we now address.

We identify the hexatic domains according to the ar-

gument of ψ_{6j} or by the gradient of its modulus, coarse-grained over a small cell, and we find consistent results with the two methods (see the SM). The average (over domains) gyration radius, R_H , is exposed in Fig. 3(b) for different N , and in Fig. 4(b), (d) for different Pe and ϕ . R_H is quite independent of the system size. In the intermediate regime $R_H \simeq t$. At a sharp crossover the evolution slows down remarkably, $R_H \simeq t^{0.13}$, a law confirmed by the analysis of the corresponding structure factor. Similar small exponents were found in the growth of order in certain pattern formation processes [34] and in the growth of hexatic order in block co-polymer systems [35]. Later R_H approaches a finite limit, R_H^s , proving the *arrested coarsening* of hexatic order, see Fig. 3(b). The snapshots in Fig. 3(c)-(f) show that hexatic domains have roughly the same size in systems of different size. The asymptotic R_H^s increases with Pe at fixed ϕ , Fig. 4(b), but does not change appreciably with ϕ at fixed Pe , Fig. 4(d), meaning that self-propulsion controls the size of the hexatic micro-domains. The inset in Fig. 4(b) unveils that $R_H^s(Pe)$ is well represented by a logarithm. This is confirmed by the exponential distributions of the individual R_H in Fig. 1: their Pe -increasing scales lead to average values compatible with those in Fig. 4(b). Finally, we did not find any correlation between the local hexatic and velocity fields nor a finite velocity correlation length, as recently observed in a similar (though athermal) ABP model as τ is increased at fixed $v = F_{act}/\gamma$ [16].

Besides the emergence of hexatic micro-domains,

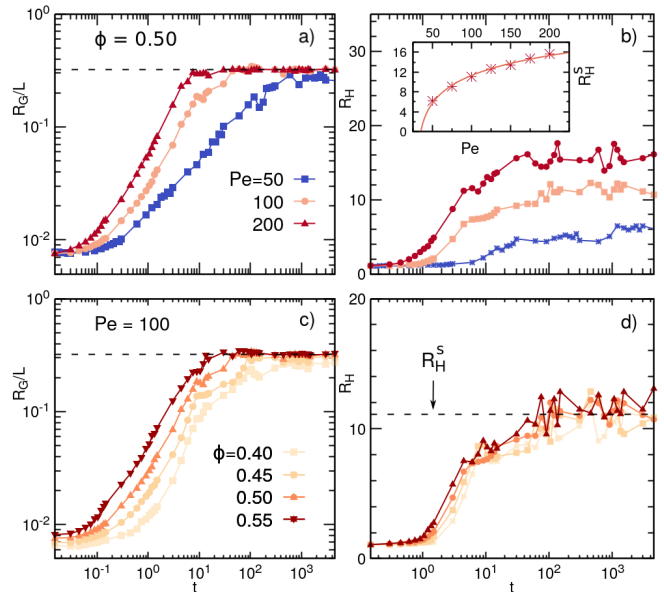


FIG. 4. Parameter dependencies of the dense phase and hexatic growing lengths. $N = 128^2$ at fixed $\phi = 0.5$ and varying Pe (a), (b); and at fixed $Pe = 100$ and varying ϕ (c), (d). Inset in (b): dependence of the asymptotic value R_H^s on Pe ; the continuous line is $R_H^s \propto \ln[Pe - a] + b$ with $a = 29.01$ and $b = -1.79$ (vanishing at the transition point).

MIPS is accompanied by the formation of gas bubbles. As illustrated in Fig. 5(a)-(c) and even more clearly in movies 1-3 (link to the movies in the SM), all bubbles have the same density (set by the lower branch of the binodal). Their averaged size, measured, for example, from their radius of gyration, R_B , increases with Pe (see SM for details). Just as the hexatic micro-domains, bubbles do not coarsen indefinitely. Figure 5(d) shows that R_B is delayed with respect to R_H , but after the transient the two quantities grow parallelly in the log-log representation indicating that they follow a similar trend until eventual saturation to a Pe-dependent value (see the SM). The R_B steady state-distribution, Fig. 5(e), decays algebraically, $P(R_B) \sim R_B^{-2.19}$ for $\phi = 0.75$, independently of Pe, until a Pe-increasing cut-off $R_B^*(\text{Pe})$. Interestingly, the system approaches the same finite R_H^s and R_B^s independently of the initial condition. This fact can be visualized in movies 2 & 3 (see the SM) where a disk and a slab drop with uniform hexatic order are used as initial states, respectively. In both cases the dense component progressively breaks into finite size domains with different orientation, leaving space for bubbles at their interfaces. Consistently, the insert in Fig. 5(d) shows the rise of R_B , and corresponding drop-off of R_H , which approach asymptotic values that are consistent with the ones obtained after a quench from disordered initial conditions.

Micro-bubbles have been predicted by a continuum model of MIPS [20], but their existence in particle-systems has not been studied yet. Micro-phase-separation in the continuum model takes place in a specific parameter regime. However, such parameters (in particular the one quantifying the term leading to the micro-bubbles) cannot be readily translated in terms of the ϕ and Pe of ABP. Here, contrarily to the mean-field calculations in [20], we observe micro-bubbles as long as MIPS takes place, both at moderate and high densities, from Pe = 40 to Pe = 200 (see Figs. 1 & 5 at $\phi = 0.25$ and 0.75, respectively, and the SM), and show that their size can be controlled by Pe.

The microscopic origin of micro-bubbles in ABP can be tracked down to the presence of topological defects (mis-coordinated particles with more or less than the 6 neighbors) mostly localized at the boundaries of the hexatic micro-domains, see Fig. 5(c) and [13]. A fluctuation is thus more likely to generate a bubble at a grain boundary than within a hexatic domain. Some of the bubbles thus generated quickly decay, while others grow and have very long life-times ($\sim 10 - 100 \tau$), of the same order as the reorganization time scale of the hexatic domains. These features are displayed in the movies (see the SM). The emergence of a finite Pe-dependent length-scale associated with the hexatic order must then be responsible for the presence of micro-bubbles as suggested by the growth kinetics of R_H and R_B , which evolve at the same very slow rate. Furthermore, the exponentially cut-off

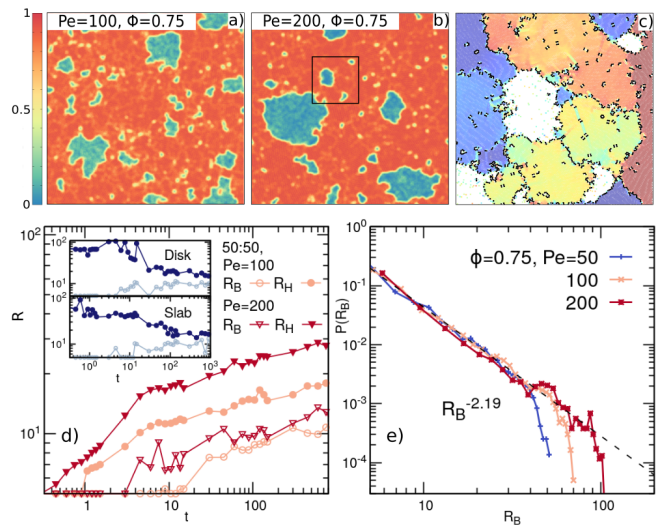


FIG. 5. **Gas micro-bubbles.** Snapshots at $\phi = 0.75$, Pe = 100 (a) and Pe = 200 (b). The color scale (left) is associated to the local density. In (c) a zoom over a sector of (b) showing hexatic domains delimited by clusters of defects (represented by black dots), where bubbles (dilute regions) are likely to emerge. (d) Growth of the bubble typical radius R_B (empty symbols) confronted to the one of the hexatic order R_H (filled symbols) for two Pe. Inset: Evolution of R_B and R_H from an initial hexatically ordered disk or slab at Pe = 100 and $\phi = 0.5$ (see movies 2 and 3 in the SM). (e) Steady-state distribution of bubble radii R_B (parameters given in the key).

algebraic distribution of bubble radii, Fig. 5(e), is intimately related to the same kind of statistics found for topological defect clusters [13].

Summarizing, we monitored the Motility-Induced Phase Separation (MIPS) of large systems of ABP. On top of the dense-dilute phase separation, governed by a $t^{1/3}$ growing length in the scaling regime, $2d$ MIPS involves another ordering mechanism controlled by activity, giving rise to a new finite characteristic length associated to hexatic order. As a result, the dense phase breaks into a mosaic of differently oriented patches. The analysis of hexatic order thus provides a new means of controlling the self-organization of active particles. The ability of active systems to sustain non-equilibrium structures and control coarsening has been reported in a variety of cases (Janus colloids, bacteria, motility assays, etc.) [27, 36–38] but has remained elusive in simple models of spherical self-propelled particles. We showed that self-propulsion and excluded volume are sufficient to arrest orientational coarsening and stabilize finite-size structures. Moreover, we proved that gas bubbles naturally appear in the interstices between different hexatically ordered patches, where topological defects favor their emergence. The bubbles' growth follows the same (delayed) pace as the one of the hexatic patches and their size also saturates to a finite value that depends on Pe but not significantly on ϕ . The statistics of cavitation bubbles is in close relation

to the one of clusters of topological defects. It would be interesting to associate these features to measurements of local pressure but these are notably difficult to carry out and lie beyond the scope of this study.

Acknowledgments. We acknowledge access to the MareNostrum Supercomputer at the BSC, Lenovo NeXtScale MARCONI at CINECA (Project INF16-field-turb) under CINECA-INFN agreement This research is supported by MIUR project PRIN 2017/WZFTZP “Stochastic forecasting in complex systems”. D. L. acknowledges funding from JIN project RTI2018-099032-J-I00 (MCI/AEI/FEDER, UE).

-
- [1] Marchetti M.C., Joanny J.F., Ramaswamy S., Liverpool T.B., Prost J., Rao M., Simha R.A., *Rev. Mod. Phys.*, **85**, 1143 (2013).
- [2] Shaebani M.R., Wysocki A., Winkler R.G., Gompper G., Rieger H., arXiv:1910.02528, (2019).
- [3] Cates M.E., Tailleur J., *Annu. Rev. Cond. Matt. Phys.*, **6**, (2015).
- [4] Romanczuk P., Bär M., Ebeling W., Lindner B., Schimansky-Geier L., *Eur. Phys. J. Spec. Topics*, **202**, (2012)).
- [5] Bialké J., Speck T., Löwen H., *Phys. Rev. Lett.*, **108**, 168301, (2012).
- [6] Fily Y., Marchetti M.C., *Phys. Rev. Lett.*, **108**, 235702, (2012).
- [7] Stenhammar J., Marenduzzo D., Allen R.J., Cates M.E., *Soft Matter*, **10**, 1489, (2014).
- [8] Levis D., Codina J., Pagonabarraga I., *Soft Matter*, **13**, 8113, (2017).
- [9] Speck T., Menzel A.M., Bialké J., Löwen H., *J. Chem. Phys.*, **142**, 224109 (2015).
- [10] Redner G.S., Hagan M.F., Baskaran A., *Phys. Rev. Lett.*, **110**, 055701, (2013).
- [11] Digregorio P., Levis D., Suma A., Cugliandolo L.F., Gonnella G., Pagonabarraga I., *Phys. Rev. Lett.*, **121**, 098003, (2018).
- [12] Klamsner J.U., Kapfer S.C., Krauth W., *Nat. Comm.*, **9**, 5045, (2018).
- [13] Digregorio P., Levis D., Cugliandolo L.F., Gonnella G., Pagonabarraga I., arXiv:1911.06366 (2019).
- [14] Paliwal S., Dijkstra M., *Phys. Rev. Res.*, **2**, 012013, (2020).
- [15] Mandal S., Liebchen B., Löwen H., *Phys. Rev. Lett.*, **123**, 228001, (2019).
- [16] Caprini L., Marconi U.M.B., Puglisi A., *Phys. Rev. Lett.*, **124**, 078001, (2020).
- [17] Stenhammar J., Tiribocchi A., Allen R.J., Marenduzzo D., Cates M.E., *Phys. Rev. Lett.*, **111**, 145702, (2013).
- [18] Wittkowski R., Tiribocchi A., Stenhammar J., Allen R.J., Marenduzzo D., Cates M.E., *Nature Comm.*, **5**, 1, (2014).
- [19] Speck T., Bialké J., Menzel A.M., Löwen H., *Phys. Rev. Lett.*, **112**, 218304, (2014).
- [20] Tjhung E., Nardini C., Cates M.E., *Phys. Rev. X*, **8**, 031080, (2018).
- [21] Liebchen B., Marenduzzo D., Pagonabarraga I., Cates M.E., *Phys. Rev. Lett.*, **115**, 258301, (2015).
- [22] Liebchen B., Marenduzzo D., Cates M.E., *Phys. Rev. Lett.*, **118**, 268001, (2017).
- [23] Mognetti B.M., Šarić A., Angioletti-Uberti S., Cacciuto A., Valeriani C., Frenkel D., *Phys. Rev. Lett.*, **111**, 245702, (2013).
- [24] Alarcón F., Valeriani C., Pagonabarraga I., Ignacio, *Soft Matter*, **13**, 814, (2017).
- [25] Solon A.P., Chaté H., Tailleur J., *Phys. Rev. Lett.*, **114**, 068101, (2015).
- [26] Liebchen B., Levis D., *Phys. Rev. Lett.*, **119**, 058002, (2017).
- [27] You Z., Pearce D.J.G., Sengupta A., Giomi L., *Phys. Rev. X*, **8**, 031065, (2018).
- [28] Cugliandolo L.F., Digregorio P., Gonnella G., Suma A., *Phys. Rev. Lett.*, **119**, 268002, (2017).
- [29] Digregorio P., Levis D., Suma A., Cugliandolo L.F., Gonnella G., Pagonabarraga I., *J. Phys.: Conf. Series*, **1163**, 012073, (2019).
- [30] Here, the MIPS critical point is located at $(Pe, \phi) \approx (32, 0.6)$.
- [31] Bray A.J., *Adv. in Phys.*, **51**, 481, (2002).
- [32] Tartaglia A., Cugliandolo L.F., Picco M., *J. Stat. Mech.*, **2018**, (2018).
- [33] Leyvraz F., *Phys. Rep.*, **383**, 95, (2003).
- [34] Cross M.C., Hohenberg P.C., *Rev. Mod. Phys.*, **65**, 851, (1993).
- [35] Vega D.A., Harrison C.K., Angelescu D.E., Trawick M.L., Huse D.A., Chaikin P.M., Register R.A., *Phys. Rev. E*, **71**, 061803, (2005).
- [36] Theurkauff I., Cottin-Bizonne C., Palacci J., Ybert C., Bocquet L., *Phys. Rev. Lett.*, **108**, 268303, (2012).
- [37] Schaller V., Weber C., Semmrich C., Frey E., Bausch A.R., *Nature*, **467**, 73, (2010).
- [38] Weber C.A., Zwicker D., Jülicher F., Lee C.F., *Rep. Prog. Phys.*, **82**, 064601, (2019).

Supplementary Material - Micro and Macro Motility-Induced Phase Separation in a two-dimensional Active Brownian Particle system

In this Supplemental Material we show additional information on the MIPS process undergone by Active Brownian Particles (ABP), following the dynamics defined in Eq. (1) in the main text, together with a detailed description of the numerical methods used for the analysis presented in the main text. The document is organized as follows: Section S1 presents three videos that illustrate the dynamic mechanisms at work. In Sec. S2 we provide snapshots, drawn in the form of heat maps of the local density, to further illustrate the structure of the system in the Motility Induced Phase Separation (MIPS) regime, and make clear the existence of cavitation bubbles. In Sec. S3 we show how the phase ordering kinetics of MIPS fulfills the dynamical scaling hypothesis, and prove that the structure factor exhibits the expected small wave-vector dependence and Porod's law beyond the first peak. Finally, in Sec. S4 we describe the clustering algorithms that we used to identify the different characteristic length scales discussed in the Letter, based on the analysis of the local surface fraction and the local hexatic order parameter.

S1. VIDEOS

Three videos reproduce the system dynamics starting from different initial states [1]. Some relevant quantities concerning the dynamics of the three videos are shown in Fig. S1, see its caption for more details.

1. Movie1 shows the entire dynamics of phase separation, starting from a random uniformly distributed configuration at the desired packing fraction, $\phi = 0.480$. The quench is done to $Pe = 200$, well within the MIPS sector of the phase diagram. The video focuses distinctly on the three dynamical regimes highlighted in Fig. 2 of the main text. The first regime of nucleation, from $t \sim 10^{-2}$ to $t \sim 5 \times 10^{-2}$, is shown with a rate of $\sim 5 \times 10^{-4}$ time

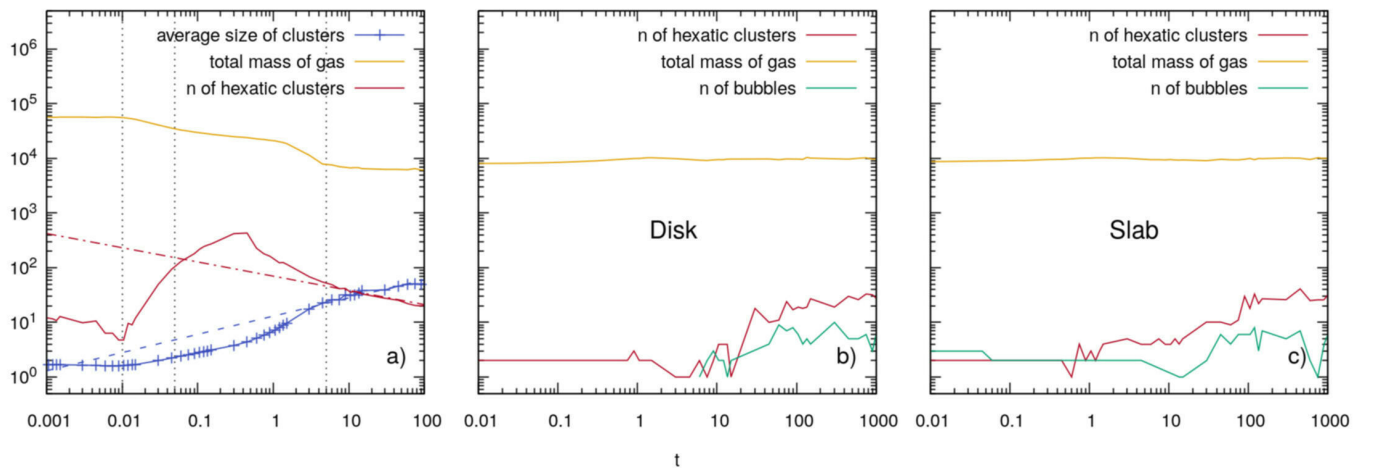


FIG. S1. (a) Average radius of droplets (blue symbols) as a function of time, evaluated as described in Sec. S3, with approximate power-law growth $R(t) \sim t^{1/3}$ in the scaling regime (dotted blue line). The yellow curve represents the total number of particles M_{gas} belonging to the gaseous phase, which, notably, reaches a plateau in the scaling regime. The red line is the evolution in time of the total number of hexatic clusters. The dashed red line represents the power-law decaying of the latter within the scaling regime, as estimated from the absence of particle exchange between the two phases and $n_H \sim M_{dense}/R_H^2 \sim t^{-0.26}$, given the measure of the growing exponent for the average hexatic radius shown in the main text. Data refer to the dynamics shown in Movie1, with a random homogeneous initial condition. Finally, the dotted vertical lines delimit the three regimes: nucleation, condensation and aggregation, and scaling. (b) Number of hexatic clusters (red line) and bubbles (green line), and total mass of the gaseous phase (yellow line), corresponding to the dynamics of Movie2, with an hexatically ordered disk as initial condition. (c) Same quantities for the dynamics of Movie3, with a slab with hexatic order as initial condition.

units per second. As confirmed quantitatively in Fig. S1(a), the number of clusters grows in this first regime, and the structure factor, see Fig. S3, begins to develop a short-wavelength peak, as a result of the formation of small clusters. Within the second regime, from $t \sim 5 \times 10^{-2}$ to $t \sim 5 \times 10^{-1}$, the condensation of particles from the gaseous phase into the clusters, and the coalescence of macroscopic clusters, contribute to the growth of the dense phase. This is corroborated in Fig. S1(a), where one observes the decrease of both the number of clusters and the total mass of the gaseous phase. This regime is shown in the movie with a rate of $\sim 5 \times 10^{-2}$ time units per second. Finally, within the dynamical scaling regime, shown with ~ 0.5 time units per second, the mass of the two phases is conserved, and the average cluster size grows due to merging of clusters (accompanied by some clusters that evaporate and break, and later recombine) as shown in Fig. S1(a).

2. Movie2 displays the evolution of a system with $\phi = 0.500$ and $Pe = 100$, starting from an initial configuration engineered as a disk with uniform local hexatic order. Positions of particles inside the disks are extracted from a stationary configuration of a system with quasi-long-range hexatic order, evolved at the same $Pe = 100$ but higher global surface fraction, which selects the right target binodal density for the dense phase in MIPS. The disk occupies half of the total area of the system, corresponding to the same amount we observe at stationarity for global $\phi = 0.500$ (see main text). The free space around the disk is filled with randomly located particles. Constant global mass of the gaseous phase during evolution from such initial state, shown in Fig. S1(b), confirms that the chosen partition of the system is the right one. The video demonstrates that the global orientational order is progressively lost: the disk breaks into pieces of smaller size, as shown by the increasing number of hexatic clusters and bubbles in between them in Fig. S1(b).
3. Movie3 presents the evolution of the same system starting now from an initial state with an ordered slab, built with the same procedure as the one used for the disk.

S2. LOCAL DENSITY MAPS

Figure S2 shows six snapshots in the form of heat maps of the local density, according to the scale in the right vertical bar, running from close packed (red) to the dilute limit (blue). These snapshots correspond to steady-state configurations of $N = 512^2$ ABPs for the different values of ϕ and Pe indicated in the key. The panels are ordered in such a way that Pe increases from left to right. On the first row the system phase separates into half dense and half dilute, while on the second row the packing fraction is just constant, $\phi = 0.75$. In all cases one clearly notices the phase separation between dense and dilute regions. Several other features can be noted as well. First, for increasing Pe , the density contrast between the two coexisting phases is more pronounced, and thus the phase boundaries (in yellowish) become sharper. Second, in all cases gas bubbles populate the dense (red) phase. Third, the bubbles have different sizes and their characteristic average size increases with Pe .

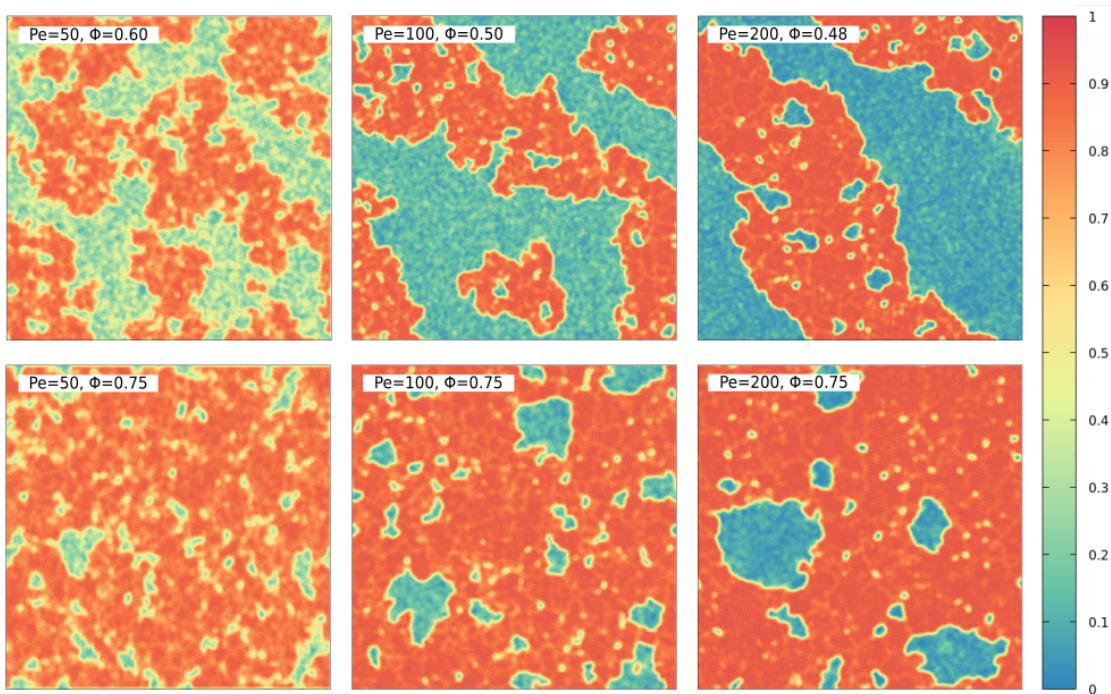


FIG. S2. Local density map of different steady-state configurations of systems with $N = 512^2$ ABP using the color scale shown in the right bar. The parameters are given as labels within each panel.

S3. DYNAMICAL SCALING

The time-dependent spherically averaged structure factor $S(k, t)$ (associated to the density-density correlations) at several times t after the quench is shown in Fig. S3. The increase in magnitude of the short wave-length peak as a function of time and its shift towards lower wave-vector values follow the large scale ordering kinetics of the system after being quenched to high activity from a randomly disordered state (see the main text for details about the quench). The location of the first peak, $\hat{k}(t)$, corresponds to the characteristic length scale in the system, the dense cluster(s) mean size, by the relation $R(t) = \pi/\hat{k}(t)$. The structure factor also shows a second peak at a time-independent wave-length, $k \sim 2\pi/\sigma_d$, that is related to the short-distance hexatic structure of the dense phase [2]. After the time scale associated to the nucleation of small aggregates from the homogeneous disordered phase, the position of this peak does not vary. This time-independence suggests that the local structure of the system does not significantly change over the scale of the first neighbor shells, while the size of the dense clusters grows. The large-scale behavior, in between the first and second peak, is in agreement with Porod's law, $S(k, t) \sim k^{-(d+1)}$, with $d = 2$ the dimensionality of the system, as expected for segregated systems with smooth interfaces between the phases [3].

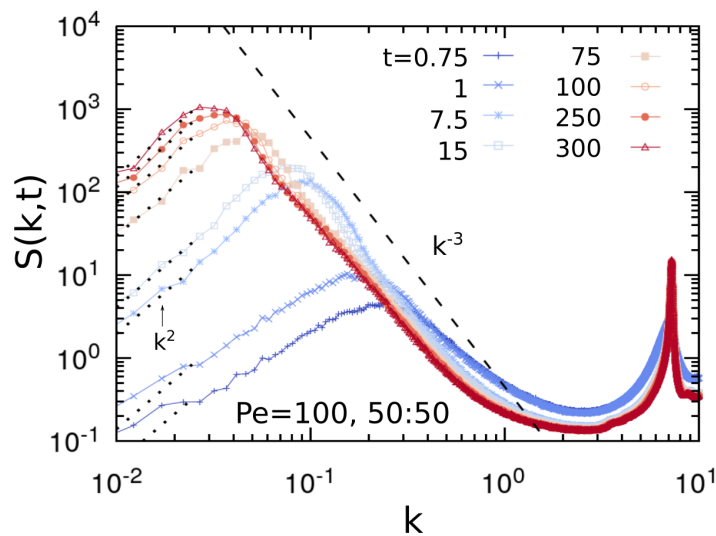


FIG. S3. Structure factor $S(k, t)$ calculated from simulations of $N = 1024^2$ ABP at $Pe = 100$ (using a 50:50 mixture) and for the different times after the quench reported in the key. The dotted lines are the k^2 growth for very small wave vector expected in the long time scaling limit. The first peak is at $\hat{k}(t) = \pi/R(t)$ with $R(t)$ the typical growing length of the dense phase. The dashed line $\sim k^{-3}$ is shown as a reference for the decay on the long-wavelength side of the peak, according to Porod's law. The second peak is located at $k \sim 2\pi/\sigma_d$ and it does vary with time.

Numerical simulations [4] suggested that MIPS in ABP verifies dynamical scaling [3], meaning that at the late stages of phase separation, the evolution of the structure factor is characterized by a single length scale:

$$S(k, t) = R(t)^d \mathcal{F}(kR(t)). \quad (\text{S1})$$

We extensively tested this hypothesis in our simulations with $N = 1024^2$ particles. We used systems made of an equal fraction of dense and dilute phases (50:50 fraction), for different Pe values. In Fig. S4 we show scaled data using Eq. (S1) and $R(t)$ extracted from the numerical data (see Sec. S4-A below). The data collapse at late times ($t \gtrsim 7.5$ in units of $1/D_\theta$) allows us to define the “scaling regime”, during which the dynamics fulfills Eq. (S1), as described in the main text. At early times dynamical scaling is not satisfied, meaning that several length scales are present in the initial growing kinetics. Indeed, we identified two other regimes before scaling sets in. In these two earlier regimes, the growth is lead by two different mechanisms described in the main text.

Finally, Furukawa showed that for conserved scalar order parameter dynamics (model B continuous field theory) the small k behavior of the scaling function $\mathcal{F}(kR(t) = x) \sim x^2$ grows from zero as k^2 , if thermal fluctuations are effective [5]. The small wave-vector structure factor of the ABP behaves in this way at long times, as shown with the dotted lines added close to the data at different times in Fig. S3. Already at $t = 15$ the long-time behaviour is

attained. (Note that in the particle system $S(\mathbf{0}, t) = N$. The first data-points in Figs. S3 correspond to the first wave-vector available, with components $2\pi/L$.)

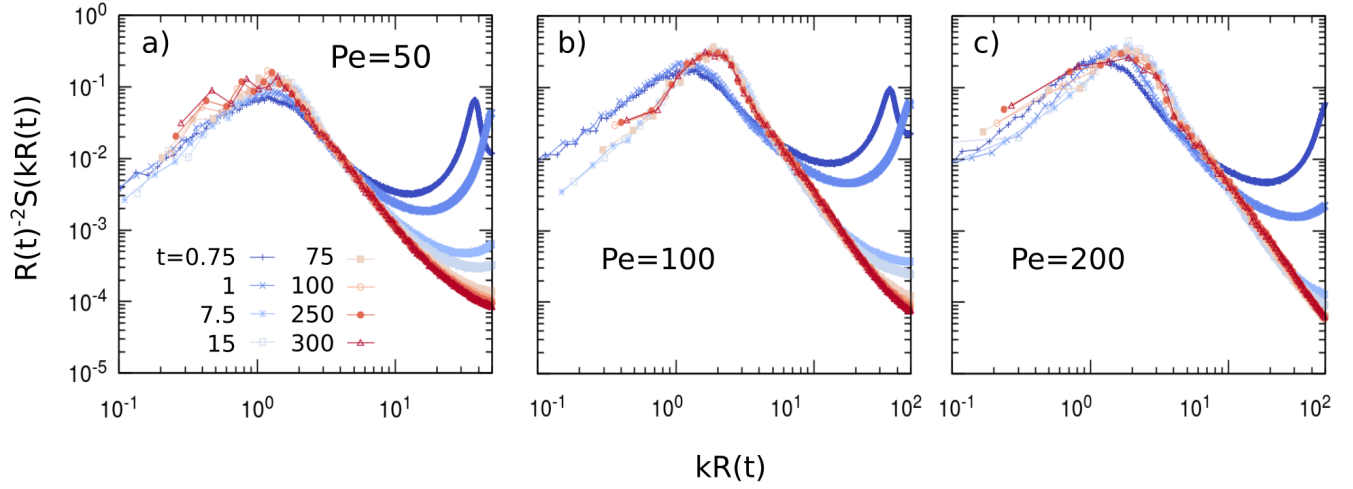


FIG. S4. Scaling of the structure factor according to the form in Eq. (S1). Data obtained from simulations of a system of $N = 1024^2$ ABP with equal fraction of the system in the dilute and dense phase. The measuring times are reported in the key in (a), and the different Pe values are indicated as labels. The data points fall on top of each other for $t > 7.5$ in all cases, showing that dynamical scaling holds at all Pe.

S4. NUMERICAL METHODS

In this Section we explain the numerical techniques that we used to identify the dense phase, or droplet, the hexatic domains and the gas bubbles.

A. Dense phase size

In Sec. S3 we used the first peak of the structure factor to identify the growing length of the dense phase. An equivalent measure of the single characteristic length in the scaling regime could be given by the first moment \bar{k} of the structure factor, over the range $[0:\pi]$,

$$R(t) = \pi/\bar{k}(t). \quad (\text{S2})$$

This quantity also allowed us to analyze the growth rate of particle clusters, the dense phase, and compare it to previous results from continuum theories.

Similar results as the ones resulting from the structure factor analysis arise from a more explicit measurement of the average size of particle aggregates, obtained by applying a standard DBSCAN algorithm to the positions of the disks [6]. DBSCAN is a clustering algorithm, which distributes points into clusters according to the local point density. We shortly outline hereafter the fundamental rules of the algorithm, in order to justify our choice of parameters.

- Given that two points are neighbors if their distance is less than a given extent ε , a point is a “core point” if it has at least n_{\min} neighbors;
- any two core points connected through a path in the neighbors network belong to the same cluster, together with their neighbors;
- points which are not cores and are not reachable from a core do not belong to any cluster.

We used $\varepsilon = 1.5\sigma_d$ and $n_{\min} = 6$ for a successful identification of the clusters (relying on previous results at different Pe values [2]). Since particles in the dense phase are locally arranged on a hexagonal lattice with local surface fraction ranging from $\phi_{\text{loc}} \sim 0.800$ at Pe = 50 to $\phi_{\text{loc}} \sim 0.900$ at Pe = 200, a circle of radius $\varepsilon = 1.5\sigma_d$ encloses the first shell of neighbors.

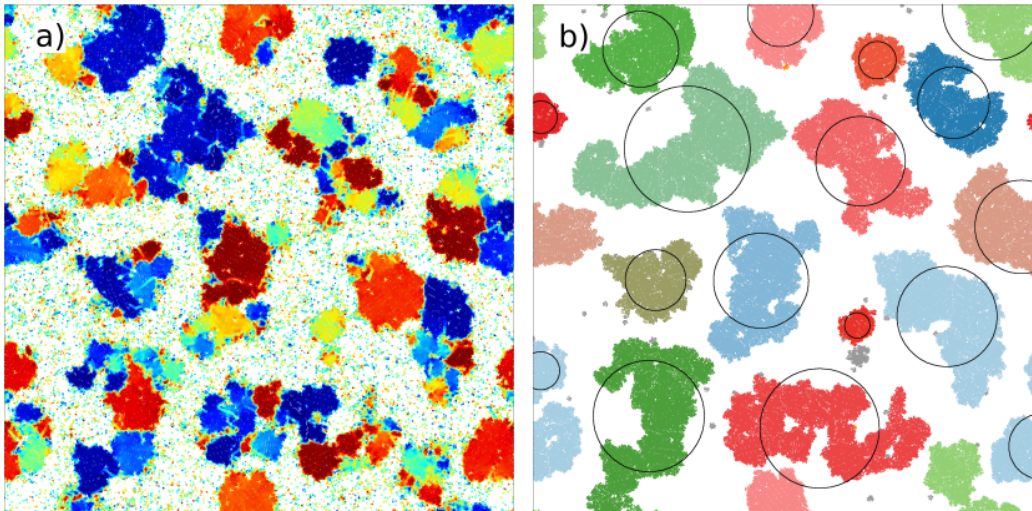


FIG. S5. (a) A configuration drawn using colors that represent the local orientational order. (b) Identification of the dense drops in (a) using DBSCAN (see text for the details). The same color is used for particles belonging to the same cluster, while isolated particles are not printed. Grey is used for small clusters, which have been discarded from the average. Black circles are centered at the center of mass of each cluster and have a radius equal to the radius of gyration of the same cluster.

An example of the performance of this algorithm is shown in Fig. S5. In (a) we show a configuration using the representation in which we paint each particle with a color associated to its hexatic order $\psi_{6,i}$ (see Fig. 1 in the main text). As in [2], red indicates maximal projection on the averaged orientation of the full sample in the ψ_6 space, and blue the maximal projection in the opposite direction, with a usual color scale in between these two extremes. One clearly observes in Fig. S5(a) phase separation between very dilute regions and rather dense ones composed of patches with different orientational order. In panel (b) we show the outcome of the use of DBSCAN to identify the clusters (each cluster is shown with a different color). The size of the clusters is then calculated from their radius of gyration,

$$r_G^i = \sqrt{s_i^{-1} \sum_{j=1}^{s_i} (\mathbf{r}_j - \mathbf{r}_{\text{cm}}^i)^2} \quad (\text{S3})$$

where s_i is the number of particles in cluster i , \mathbf{r}_j the positions of particles belonging to the cluster, and \mathbf{r}_{cm}^i its center of mass. A black circle, centered at the center of mass and with radius r_G^i , is drawn on each cluster. We then monitor the average radius of gyration $R_G(t)$ obtained after averaging over all the clusters: $R_G(t) = N_C^{-1} \sum_i r_G^i$, N_C being the total number of clusters in the system.

Although the algorithm is quite reliable on the clusters' identification, it is however not able to distinguish between macroscopic clusters leading the coarsening and very small aggregates, the latter being not stable since they continuously arise and evaporate within a timescale of a few simulation time-steps. In order to avoid their impact on the system averages, we discard, as a “rule of thumb”, all the clusters containing less than 5% particles with respect to the largest one.

B. Hexatic domains

Large dense clusters do not always have hexatic order to the scale of their whole size [2] but, instead, they are arranged in a “polycrystal” or “mosaic” of hexatically ordered domains, with almost uniform local hexatic parameter $\psi_{6,i} = N_i^{-1} \sum_j e^{i6\theta_{ij}}$ in their interior. We describe below two methods used to measure the average size of these domains, which yield consistent results. We either use a *clustering by argument* approach or a *clustering by gradient* one, to first identify hexatic domains, and then measure their size. Both methods are applied to the particles in the dense phase only, which are previously selected by the application of DBSCAN, as described in Sec. S4-A.

1. Clustering by argument.

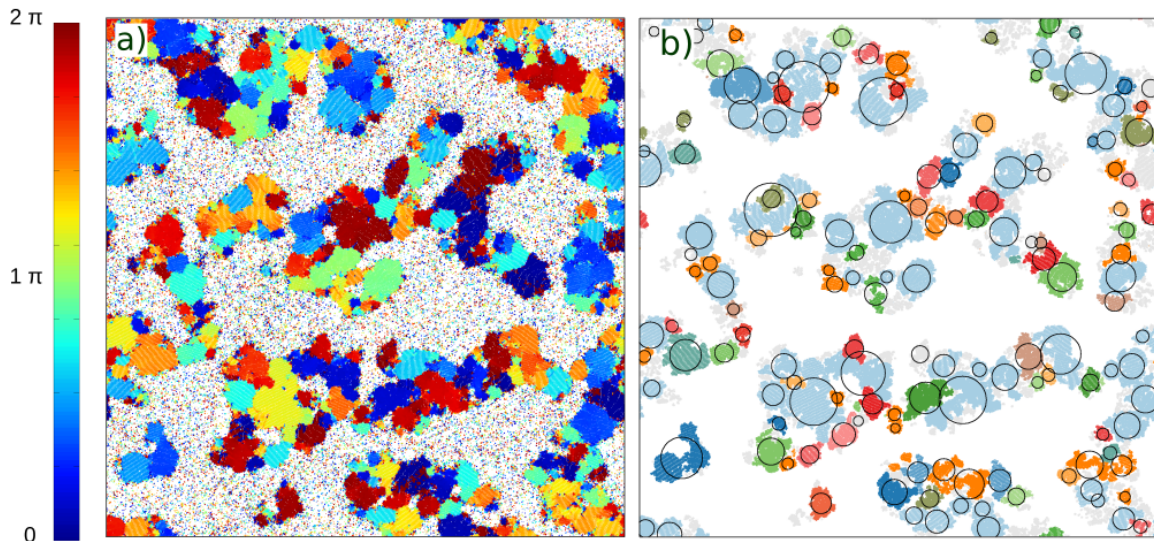


FIG. S6. Identification of hexatic domains using the argument of the local hexatic order parameter $\psi_{6,i}$. (a) Hexatic color map (see details in the main text). (b) Same system, split according to the binning of the hexatic orientation. Black circles are centered at the center of mass of each hexatic domain and have a radius equal to their radius of gyration.

Within this approach we discretize the range $[0:2\pi]$ of the argument of $\psi_{6,i}$ into n bins and we split the system accordingly. We then apply the DBSCAN algorithm to each part of the system separately and we discard, according to the rule of thumb introduced in Sec. S4.A, the clusters with less than 5% particles of the largest one. The two steps are shown in Fig. S6. We verified that the results depend only weakly on n within the range $n = 4, \dots, 10$, as shown in Fig. S8(a). We used $n = 6$ for all the measures presented in this work.

2. Clustering by gradient.

As an alternative approach to separate hexatic domains, we developed a criterion based on the spatial gradient of the argument of the local hexatic parameter. We first coarse-grain the local hexatic order parameter on a square grid of spacing $d = 5\sigma_d$, being such coarse-graining length smaller than the typical size on any hexatic domain. Then we calculate the gradient of the coarse-grained $\text{Arg}(\psi_6^{i,j})$. We then associate to each grid point a ‘0’ or ‘1’ if $|\nabla \text{Arg}(\psi_6^{i,j})|$ is larger or smaller than a certain threshold, which here we fixed to $\text{th}_{grad} = 0.2$ (in units of $1/\sigma_d$), which is approximately the 10% of the typical range of the gradient modulus. Grid points labeled with a ‘1’ are considered to belong to an hexatic domain. We then apply a DBSCAN algorithm to the grid points with $|\nabla \text{Arg}(\psi_6^{i,j})| < \text{th}_{grad}$ in order to identify the hexatic domains. Compared to the previous DBSCAN algorithm, in this case we select only the first eight neighbors for each grid point, and $n_{\min} = 4$. The radius of gyration is evaluated from the positions of the grid points. Such approach is graphically summarized in Fig. S7.

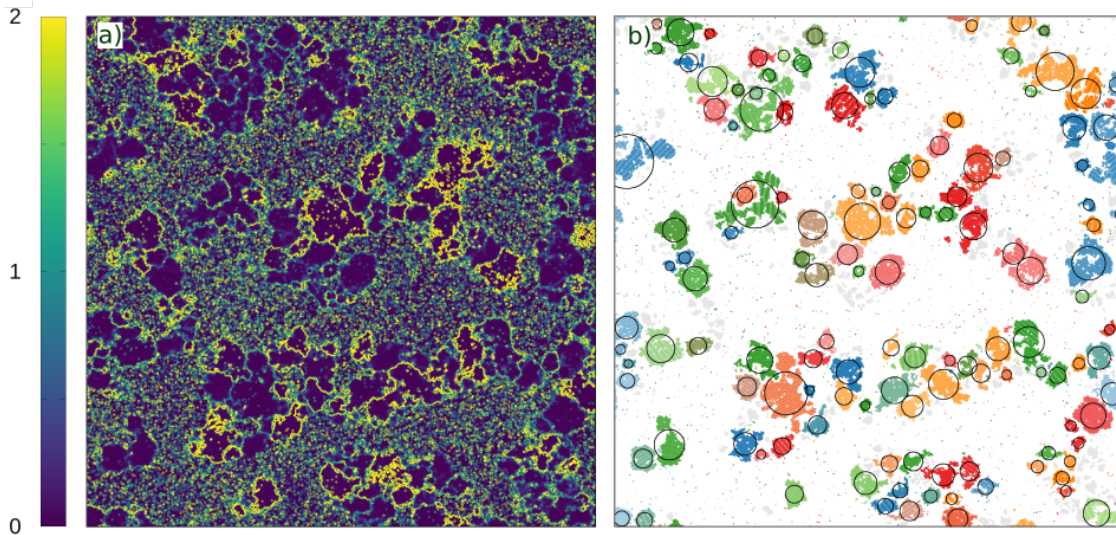


FIG. S7. Identification of hexatic domains using the spatial gradient of $\text{Arg}(\psi_6)$. (a) Gradient field computed over a square grid of side σ_d . (b) Hexatic domains, as identified from the lattice DBSCAN applied to regions in (a) where $|\nabla(\text{Arg}(\psi_6))| < 0.2$.

In Fig. S8(b) we compare the two methods described above to identify hexatic domains. We plot the averaged radius of gyration of the hexatic domains found with each technique and we show that the results are consistent. In the main text we present results found with the clustering by argument method only, with $n = 6$.

C. Bubble identification

In order to identify the bubbles we first coarse-grain the system’s local surface fraction over the length $d = 5\sigma_d$. Specifically, we divide the system area into a grid of square cells with side d , we set to 1 all the cells with average surface fraction ϕ_i below a threshold $\text{th}_\phi = 0.65$, and to 0 the ones for which $\phi_i > \text{th}_\phi$. The value of th_ϕ has been chosen to trace the dense droplets contour into the grid as accurately as possible. Bubbles are then identified by means of the lattice-DBSCAN described above, as illustrated in Fig. S9. The coarse-graining length d we used is large enough to cut off all the small bubbles of size of the order of σ_d . The latter arise from extended defects inside the dense phase (particularly across the boundaries between different hexatic domains), and are not relevant to the

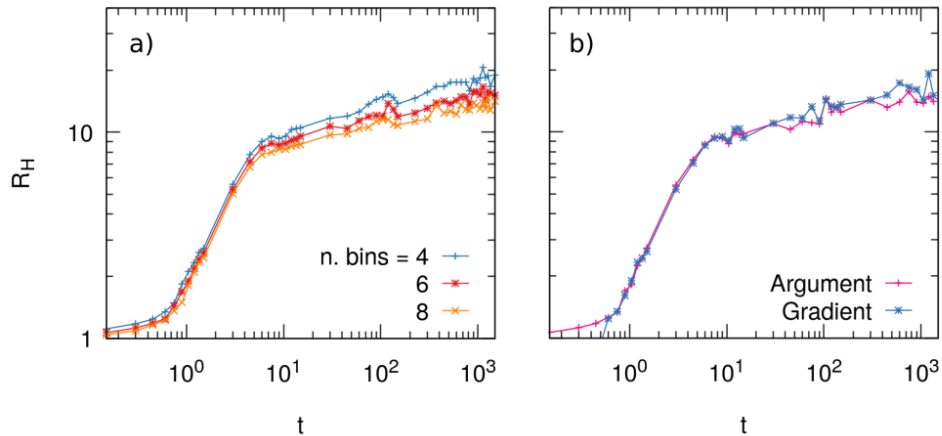


FIG. S8. The average size of clusters with the same hexatic order as a function of time. (a) Clustering by argument method: comparison between results obtained from a single simulation, using different number of bins for the discretization of the argument. (b) Comparison of results obtained using the clustering by argument (with $n = 6$) and clustering by gradient methods.

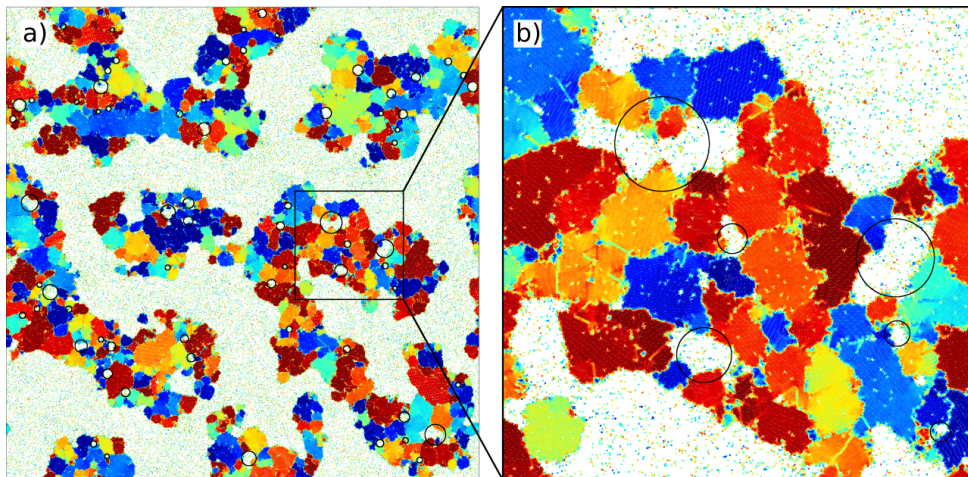


FIG. S9. (a) Hexatic map of a system with $N = 1024^2$ particles, $Pe = 200$ and $\phi = 0.480$. Black circles are centered at the center of mass of each bubble, and have radius equal to their radius of gyration R_B . (b) Zoom over the black squared area in panel (a).

large-scale phenomenon we aim to address. Finally, we also discard all the bubbles which span the whole system along either the x or the y axis, constituting the gaseous phase of the segregated system.

S5. DYNAMICAL SCALING FOR HEXATIC GROWTH

We verify, by means of a spectral analysis of the modulus of the local hexatic order parameter, that the eventually arrested hexatic order growth satisfies the dynamical scaling hypothesis over the same time regime for which the local density does, as shown in Sec. S3. This is the regime that we called “scaling” in the main text and in which the hexatic patches grow in time very slowly, with a power law with exponent that we estimated to be ~ 0.13 for $Pe = 100$ and half and half dense and dilute components but could be slightly different for these or other parameters.

Concretely, we computed the following quantity

$$S_H(\mathbf{k}) = \frac{1}{N} \langle |\psi_6|_{\mathbf{k}} |\psi_6|_{-\mathbf{k}} \rangle, \quad (\text{S4})$$

where $|\psi_6|_{\mathbf{k}}$ is the Fourier transform of the modulus of the local hexatic order parameter, defined for each particle as described in the main text. The results, for the spherically averaged quantity, are shown in Fig. S10(a) for Pe

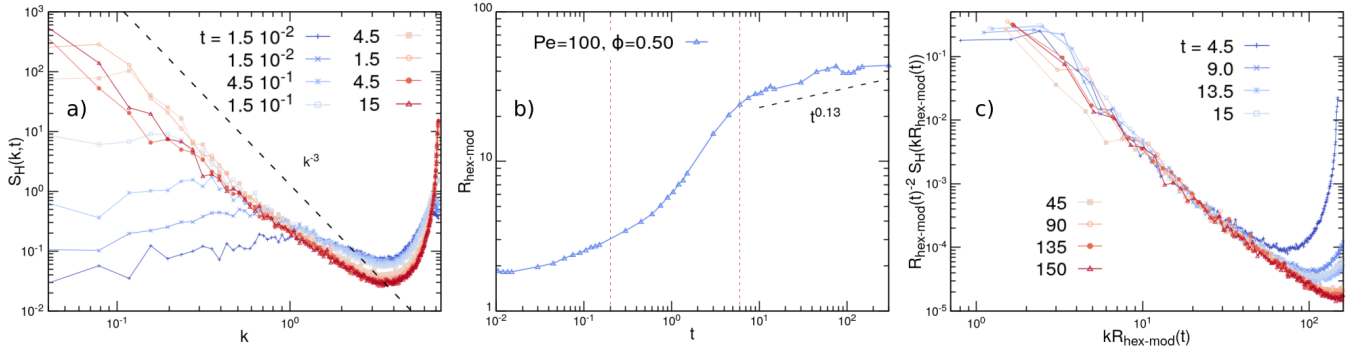


FIG. S10. (a) Hexatic modulus structure factor, as defined in Eq. (S4), in a system with $Pe = 100$ and $\phi = 0.500$. (b) Average hexatic size, computed as π/\bar{k} from the first moment \bar{k} of $S_H(k, t)$. The dashed black line $\sim t^{0.13}$ is shown next to the data. It is the growth law found from the measurement of the averaged radius of gyration of the hexatic patches presented in the main text. (c) Scaled hexatic structure factor following a scale-free shape.

$= 100$, $\phi = 0.500$ and different times spanning the entire dynamical range, from the disordered initial configuration to stationarity. Alongside the high wave-vector peak at $k \sim 2\pi$, which is related to the structure of the first neighbor shells, the hexatic modulus structure factor develops a low wave-vector peak. This represent hexatic domains and its location is shifted, from $k \sim 0.1$ at the early growing stages, to the left as time increases and the hexatic patches grow, reaching $k \sim 0.01$ at the beginning of the last stationary regime. The inverse of the first moment of S_H , which we call $R_{\text{hex-mod}}(t)$, is shown Fig. S10(b). It consistently shows the hexatic coarsening, and it very well agrees with our results on the power-law growth in the scaling regime, obtained from the analysis of the averaged gyration radius of the micro-domains. The decay of S_H from the hexatic peak towards lower wave-vectors satisfies the Porod’s law (see Sec. S3) with $d = 2$, which allows us to formulate the right scaling hypothesis. Figure S10(c) demonstrates the scaling of the structure factor, using the typical length-scale $R_{\text{hex-mod}}(t)$.

-
- [1] <https://www.dropbox.com/sh/1f2y9tsxbgzto9r/AAABgXE0mVixfwziBAzdYWhZa?dl=0>
[2] Digregorio P., Levis D., Suma A., Cugliandolo L.F., Gonnella G., Pagonabarraga I., Phys. Rev. Lett., **121**, 098003, (2018).
[3] Bray A.J., Adv. in Phys., **51**, 481, (2002).
[4] Stenhammar J., Marenduzzo D., Allen R.J., Cates M.E., Soft Matter, **10**, 1489, (2014).
[5] Furukawa H., Phys. Rev. B, **40**, 2341, (1989).
[6] Ester M., Kriegel H.P., Sander J., Xu X., in *Proceedings of the Second International Conference on Knowledge Discovery and Data Mining*, (1996).